



**HAL**  
open science

## Formation and crystal growth of needle-like rutile in glass- ceramics

Shuai Li, Yinsheng Xu, Xianghua Zhang, Ping Lu

► **To cite this version:**

Shuai Li, Yinsheng Xu, Xianghua Zhang, Ping Lu. Formation and crystal growth of needle-like rutile in glass- ceramics. *Journal of the European Ceramic Society*, 2022, 42 (7), pp.3313-3320. 10.1016/j.jeurceramsoc.2022.02.013 . hal-03629967

**HAL Id: hal-03629967**

**<https://hal.science/hal-03629967>**

Submitted on 8 Apr 2022

**HAL** is a multi-disciplinary open access archive for the deposit and dissemination of scientific research documents, whether they are published or not. The documents may come from teaching and research institutions in France or abroad, or from public or private research centers.

L'archive ouverte pluridisciplinaire **HAL**, est destinée au dépôt et à la diffusion de documents scientifiques de niveau recherche, publiés ou non, émanant des établissements d'enseignement et de recherche français ou étrangers, des laboratoires publics ou privés.



Distributed under a Creative Commons Attribution - NonCommercial 4.0 International License

## Formation and crystal growth of needle-like rutile in glass- ceramics

Shuai Li,<sup>1</sup> Yinsheng Xu,<sup>2</sup> Xianghua Zhang,<sup>2, 3</sup> Ping Lu,<sup>1, 2, \*</sup>

<sup>1</sup> School of Materials Science and Engineering, Wuhan University of Technology,

Wuhan 430070, China

<sup>2</sup> State Key Laboratory of Silicate Materials for Architectures, Wuhan University of

Technology, Wuhan 430070, China

<sup>3</sup> ISCR (Institut Des Sciences Chimiques de Rennes) - UMR 6226, CNRS, Univ

Rennes, 35000 Rennes, France

### Abstract

Glass-ceramic, which has negligible dielectric loss, high mechanical strength, excellent drop resistance, low CTE, and low density for lightweight design, is the best option for the back cover of mobile devices in the 5G era. Herein, the effect of P<sub>2</sub>O<sub>5</sub> on the phase separation and crystallization of MgO–Al<sub>2</sub>O<sub>3</sub>–SiO<sub>2</sub>–TiO<sub>2</sub> glass-ceramics is studied. The incorporation of P<sub>2</sub>O<sub>5</sub> in the glass structure leads to phase separation, in which the P and Mg-enriched phase was formed in the glass matrix, and promotes the increase of  $T_g$ . With the increase of P<sub>2</sub>O<sub>5</sub> content, the precipitated crystals change significantly. First, the silicate crystals (Mg<sub>2</sub>SiO<sub>4</sub>) disappear, whereas the phosphate crystals (LiMgPO<sub>4</sub>) emerge when 2 mol% P<sub>2</sub>O<sub>5</sub> is introduced. Second, titanate crystal (MgTi<sub>2</sub>O<sub>5</sub>) can not be observed when 4 mol% P<sub>2</sub>O<sub>5</sub> is introduced. The Ti<sub>5</sub>O<sub>9</sub> crystals

---

\* Corresponding author:

Email: [Lupingwh@whut.edu.cn](mailto:Lupingwh@whut.edu.cn); Phone: +86 13476073984

appear simultaneously with  $\text{LiMgPO}_4$  crystals and transform to rutile  $\text{TiO}_2$  crystals at high temperature. Interestingly, the needle-like rutile  $\text{TiO}_2$  crystals, which is 300 nm long and 20 nm wide, have been found in a glass with 4 mol%  $\text{P}_2\text{O}_5$ . The large L/D ratio of needle-like crystals increases the hardness significantly from 6.08 GPa to 7.14 GPa. Similar to other fiber reinforced composites, this needle-like crystals provide a new strategy to improve the mechanical properties of glass ceramics.

**Keywords:** glass- ceramics, needle-like, rutile

## 1. Introduction

Glass-ceramic, which is prepared by controlled crystallization from the inorganic glass,<sup>1</sup> has negligible dielectric loss; thus, it has little effect on the transmission of electromagnetic signals and good applicability for 5G communications. It also exhibits remarkable characteristics including high mechanical strength, low CTE, and low density for lightweight design.<sup>2-4</sup> Meanwhile, compared with traditional materials, glass-ceramics are more suitable for wireless charging technology. Thus, glass-ceramic is the best option for back and front cover materials of mobile devices. Moreover, with the continuous improvement of mobile phone functions, the usage frequency of mobile phones has gradually increased, which has increased the probability of mobile phones falling, resulting in higher requirements for mobile phone packaging materials.

In recent years, Corning company launched the first glass-ceramic used in

iPhone 12 back and front cover materials, setting off a frenzy of research in the related field. Among the most studied glass-ceramics, the MgO–Al<sub>2</sub>O<sub>3</sub>–SiO<sub>2</sub> (MAS) system is known to be suitable for the production of high-strength glass-ceramics. Peter *et al.* obtained MAS glass ceramics with hardness of 9.5 GPa by adjusting the treatment procedure.<sup>5</sup> Han *et al.* obtained MAS glass ceramics with hardness of 7.94 GPa and compressive strength of 509 MPa by adjusting the nucleating agent.<sup>6</sup> However, the main crystal phases of the current MAS glass-ceramic system are bulk crystals with relatively small length and diameter. Meanwhile, fiber reinforcement is a commonly used methods to improve mechanical properties. The mechanical properties of glass can be improved by using needle-like crystals.<sup>7, 8</sup> Höland *et al.*, found that the precipitation of needle-like fluorapatite Ca<sub>5</sub>(PO<sub>4</sub>)<sub>3</sub>F crystals in glass-ceramics improved the durability of glass-ceramics.<sup>7</sup> Bansal *et al.* prepared unidirectional chemical-vapor-deposited silicon-carbide-fiber-reinforced glass ceramics by hot pressing, resulting in a flexural strength of 825 MPa.<sup>8</sup>

Three polymorphs of TiO<sub>2</sub>, rutile, anatase and brookite have been found in nature, among which rutile crystals have a needle-like morphology. Yin *et al.* found that well-crystallized needle-like rutile nano-crystals possessed higher photocatalytic activities than anatase crystals under visible light irradiation with wavelength of >400 and/or >510 nm.<sup>9</sup> However, the research on needle-like rutile crystals primarily focuses on photocatalysis, and its precipitation as the crystal phase has little influence on glass-ceramics.

In this work, the needle-like rutile  $\text{TiO}_2$  crystals were precipitated in  $\text{MgO-Al}_2\text{O}_3\text{-SiO}_2\text{-TiO}_2$  (MAST) glass by one-step heat treatment (HT). The effects of  $\text{P}_2\text{O}_5$  on MAST glass forming and crystallization behavior were investigated. Furthermore, the structure and surface morphology of the precipitated crystals were evaluated.

## 2. Experimental section

### 2.1 Glass synthesis

The chemical composition of the studied glass was  $(60.5-x) \text{SiO}_2\text{-}11.5 \text{Al}_2\text{O}_3\text{-}x \text{P}_2\text{O}_5\text{-}8 \text{MgO}\text{-}4 \text{TiO}_2\text{-}11 \text{Na}_2\text{O}\text{-}5 \text{Li}_2\text{O}$  ( $x=0, 2, 4$ , in mol.%, labeled as P0, P2, P4). The starting materials were analytical grade reagents, including  $\text{SiO}_2$  ( $\geq 99.0\%$ ),  $\text{Al}_2\text{O}_3$  ( $\geq 99.0\%$ ),  $\text{MgO}$  ( $\geq 99.5\%$ ),  $\text{TiO}_2$  ( $\geq 99.0\%$ ),  $\text{Na}_2\text{CO}_3$  ( $\geq 99.0\%$ ),  $\text{Li}_2\text{CO}_3$  ( $\geq 99.0\%$ ), and  $\text{Na}_2\text{HPO}_4$  ( $\geq 99.0\%$ ), which were melted in 90% Pt/10% Rh crucibles (covered with a Pt lid) in an electric furnace (Carbolite BLF 1800 furnace) at  $1620^\circ\text{C}$  for 3 h. Then, the melt was quenched by pouring onto a copper plate and immediately pressing by a second plate to maximize the cooling rate. After cooling down to room temperature, as-quenched glasses were heat-treated with different crystallization temperatures from  $610^\circ\text{C}$  to  $890^\circ\text{C}$  for 2 h.

### 2.2 Characterization

Differential scanning calorimetry (DSC) data were collected with 40 mg of

powder specimen using a Simultaneous Thermal Analyzer (STA 449 F1, Netzsch) in the temperature range of 40 °C–1000 °C at a heating rate of 10 K/min under a constant flow of nitrogen gas. The glass transition temperature  $T_g$  and crystallization temperature  $T_p$  were determined from DSC curves.

The crystalline phase of glass and glass ceramics was observed by X-ray diffraction (XRD, PAN-alytical X'Pert Pro; Cu  $K_\alpha$ : 40 kV, 40 mA;  $2\theta=5^\circ$ - $80^\circ$ ; scanning speed= $10^\circ$ /min; step size =  $0.01^\circ$ /s). The powder sample was used for XRD test.

A laser confocal microscopic Raman spectrometer (DXR, Thermo Electron, USA) equipped with a 532 nm laser was utilized for structural analysis of glass samples operating at 100 mW. The spectra were acquired on the clean surface of the quenched glass from  $200\text{ cm}^{-1}$  to  $1200\text{ cm}^{-1}$  at room temperature.

Images obtained from a field emission scanning electron microscope (SEM, Hitachi S-4800, 5 kV) were collected on unpolished glass-ceramic samples coated with  $\sim 4$  nm thick platinum. Before spraying platinum, the glass-ceramics were etched with 2 Vol.%  $\text{HNO}_3$  solution for 30 s and cleaned by ultrasonic bath. A Talos F200S scanning transmission electron microscope (STEM) operating at 200 keV was used to understand the compositional and microstructural evolution in transparent glass ceramics. The point resolution in STEM mode was 0.25 nm. The specimens for STEM analysis were prepared by using a multifunctional beam ion thinning apparatus. (Gatan PIPS 695). Sample processing is achieved by bombarding the sample with

accelerated ions to sputter the surface atoms, with specimen thickness of 20 nm.

The Vickers hardness ( $H_V$ ) was obtained using a microhardness Vickers tester (Q10A+, QNESS, Austria) in air atmosphere at room temperature. For block samples, polished surfaces were exposed through embedding the samples into the resin and careful grinding. Using an indentation load of 1.96 N for a dwell time of 10 s,  $H_V$  is the average value of the test results over 10 times.

### 3. Results

#### 3.1 DSC analysis

DSC curves of these three samples are shown in Fig. 1.  $T_g$  increased from 580 °C to 638 °C with the increase of  $P_2O_5$  concentration. For the  $P_2O_5$ -free glass, two distinct crystallization peaks at 667 and 801 °C can be observed. With the increase of  $P_2O_5$  concentration, the integrated area of the first crystallization peak decreased, and then disappeared. Meanwhile, the second crystallization peak vanished when the concentration of  $P_2O_5$  was 2 mol%. When the concentration of  $P_2O_5$  reached 4 mol%, a new crystallization peak at 735 °C emerged.

#### 3.2 X-Ray powder diffraction results

Fig. 2 presents the XRD-patterns of as-quenched glasses heattreated with different crystallization temperatures for 2 h. As shown in Fig. 2A, weak diffraction peaks corresponding to  $Mg(Ti_2O_5)$  crystals (PDF: 89-6944) appear when the P0 glass

heat-treated at 730 °C for 2 h. With the increase of HT temperatures, the peak intensity of these diffraction peaks increased. When the HT temperature reached 850 °C,  $\text{Mg}_2(\text{SiO}_4)$  crystals (PDF: 89-5130) can be observed. For sample P2 (2 mol%  $\text{P}_2\text{O}_5$ ), the same crystallization behavior can be found at 730 °C (Fig. 2B). With the increase of temperatures, a new diffraction peak ( $2\theta=23^\circ$ ) appeared at 770 °C, whereas the other two new peaks ( $2\theta=27^\circ$  and  $38^\circ$ ) appeared at 810 °C. Finally,  $\text{Mg}(\text{Ti}_2\text{O}_5)$  (PDF:89-6499) and  $\text{LiMgPO}_4$  (PDF:84-0342) crystals co-existed in the P2 glass ceramic. For sample P4 (4 mol%  $\text{P}_2\text{O}_5$ ), the crystallization behavior was totally different (Fig. 2C). Some diffraction peaks ( $2\theta=21.91^\circ$ ,  $25.61^\circ$ ,  $30.25^\circ$ ) initially increased and then decreased, whereas some other peaks ( $2\theta=20.89^\circ$ ,  $23^\circ$ , and  $32.69^\circ$ ) increased with the increase of HT temperatures. Interestingly, phase transformation occurred, corresponding to the transformation of  $\text{Ti}_5\text{O}_9$  crystals into rutile crystals ( $\text{TiO}_2$ , PDF:87-0710). Meanwhile, the diffraction peaks of  $\text{LiMgPO}_4$  crystals suddenly increase with the appearance of  $\text{TiO}_2$  crystals.

### 3.3 Microstructure

Raman spectroscopy was adopted to analyze the quenched samples and obtain the structural characteristics of the samples. Fig. 3 shows the Raman spectra of the three samples in the range of 200-1200  $\text{cm}^{-1}$ . Four broad vibration bands appeared at 472, 585, 895 and 1070  $\text{cm}^{-1}$  for the P0 samples. When the concentration of  $\text{P}_2\text{O}_5$  reached 2 mol% (P2), the four vibration bands still existed, but the intensity of the vibration band at 1070  $\text{cm}^{-1}$  was weakened and a new Raman band appeared at 973

$\text{cm}^{-1}$ . When the concentration of  $\text{P}_2\text{O}_5$  reached 4 mol% (P4), the Raman band at  $1070 \text{ cm}^{-1}$  disappeared and the one at  $973 \text{ cm}^{-1}$  was further enhanced with a new sharp peak at  $959 \text{ cm}^{-1}$ . Such a change of vibration band at  $973 \text{ cm}^{-1}$  and  $1070 \text{ cm}^{-1}$  associating with  $\text{P}_2\text{O}_5$  will be fully expounded in the Discussion section.

Figs. 4A–4C, Figs. 4D–4F, and Fig. 5 show the surface morphology after corrosion of the P0, P2, and P4 glass-ceramics prepared at different temperatures. When the P0 sample was isothermally heat treated at  $610 \text{ }^\circ\text{C}$  for 2 h, the microstructure of  $\text{P}_2\text{O}_5$ -free heat-treated glasses (Fig. 4A) concurred with their XRD data showing a typical homogeneous amorphous characteristic. As shown in Fig. 4B, dense granular crystals appear in sample P0 at  $730 \text{ }^\circ\text{C}$ . When the HT temperature reached  $890 \text{ }^\circ\text{C}$  (Fig. 4C), the plate-like crystals appeared in the P0 sample.

As shown in Fig. 4D, holes of different geometries, ranging from approximately 30 nm to 70 nm, are visible. In addition, small particles of approximately 15 nm can be seen as agglomerates at different locations of the sample. As shown in Fig. 4E, dense crystals appeared in P2 samples with crystal sizes of approximately 10 nm–20 nm when the HT temperature reached  $730 \text{ }^\circ\text{C}$ . As shown in Fig. 4F, the sample was corroded deeply, showing granular crystals with a short L/D ratio at  $890 \text{ }^\circ\text{C}$ .

As shown in Fig. 5, large holes appeared in the erosion morphology of all samples. After HT at  $610 \text{ }^\circ\text{C}$ , only a few small particles with a size of approximately 10–20 nm were found (Fig. 5A). When the HT temperatures increased to  $730 \text{ }^\circ\text{C}$  and  $770 \text{ }^\circ\text{C}$ , dense particles appeared in the sample (Figs. 5B and 5C). By contrast, the

microstructure of the GC heat treated at 810 °C (Fig. 5D) showed some needle-like crystal phases. When the HT temperature was raised to 890 °C (Fig. 5E), the crystal dimensions grows to approximately 300 nm×20 nm; the large L/D ratio of needle-like crystals was uniformly distributed inside sample P4.

Based on the XRD and SEM results, the P4 sample heattreated at 890 °C for 2 h was further investigated for their microstructural evolution using TEM. Based on the STEM image (Fig. 6) recorded using a HAADF detector, two different crystals (spherical and needle-like crystals) appeared with bright contrast in the dark glass matrix. We performed EDS analysis of these two crystals and the glass matrix. The result shows that the Ti atoms aggregate in the needle-like crystals (Fig. 6, area 1), whereas the Mg and P atoms aggregate in the spherical crystals (Fig. 6, area 2). The glass matrix comprises Si, Al, and O (Fig. 6, area 3) with Si being the main constituent.

Fig. 7 shows STEM image and the corresponding elements mapping of the P4 heattreated at 890 °C for 2 h. Evidently, Ti atoms were enriched at the positions of needle-like crystal phases. P and Mg atoms were enriched at the positions of spherical crystal phases. Moreover, Si and Al atoms were distributed homogeneously in the glass matrix.

Fig. 8 shows the high-resolution TEM images and selected area electron diffraction (SAED) pattern of needle-like and cluster-like crystals, respectively. Well-resolved lattice fringes with a spacing of 0.322 nm can be observed (Fig. 7A).

The diffraction pattern of SAED depicted the (110) and (101) planes of rutile (Fig. 7B). For the spherical crystals, the HRTEM showed two distinct lattice fringes with a spacing of 0.248 and 0.344 nm, corresponding to the (311) and (201) planes of  $\text{LiMgPO}_4$  (Figs. 7C and 7D). These lattice spacing were obtained by measuring 10 consecutive lattice spacings, and then calculating on average. The bright ring in the SAED diffraction pattern indicated the amorphous nature of the glass matrix.

Fig. 9 shows that the Vickers hardness of the P4 sample increases significantly with the increase of HT temperature. In particular, the Vickers hardness increased from 6.56 GPa to 7.14 GPa when the HT temperature increased from 850 °C to 890 °C.

#### 4. Discussion

As the  $\text{P}_2\text{O}_5$  content in the sample gradually increases from 0 to 2 mol% and 4 mol%,  $T_g$  gradually increases from 580 °C to 588 °C and 638 °C. When the  $\text{P}_2\text{O}_5$  content is relatively small in the glass, the degree of polymerization of the glass can be increased, resulting in an increase in  $T_g$ . The crystallization enthalpy of the first crystallization peak ( $T_{p1}$ ) of the P0 sample is 5.95 J/g, which is larger than that of the P2 sample (3.06 J/g). Moreover,  $T_{p1}$  of the P4 glass vanished, indicating that the first precipitated crystals have been restrained with the addition of 4 mol%  $\text{P}_2\text{O}_5$ .

As shown in Fig. 2, all three samples have evident crystallization peaks in the XRD patterns when the samples were heat treated at 730 °C for 2 h. The precipitated

crystals represented by the first crystallization peak in the DSC curve of the P0 and P2 samples are  $\text{Mg}(\text{Ti}_2\text{O}_5)$ . However, the P0 sample has sharper crystallization peaks than the P2 sample, indicating that the  $\text{Mg}(\text{Ti}_2\text{O}_5)$  crystals in the P0 sample is easier to precipitate, which is consistent with the result of DSC. When the P4 sample was heat-treated at 730 °C for 2 h, the crystallization peaks of  $\text{Ti}_5\text{O}_9$  and  $\text{LiMgPO}_4$  crystals appeared. When the HT temperature increased to 770 °C, the intensity of the  $\text{Ti}_5\text{O}_9$  crystal devitrification peak in the P4 sample reached the highest. Then the intensity of the  $\text{Ti}_5\text{O}_9$  crystal crystallization peak gradually decreased with the increase of the HT temperature. When the HT temperature reached 890 °C, the  $\text{Ti}_5\text{O}_9$  crystal crystallization peak completely disappeared. Meanwhile, when the HT temperature reached 810 °C, the crystallization peaks of  $\text{TiO}_2$  crystals emerged and became stronger with the increase of HT temperature. Combined with the SEM test results of the P4 sample (Fig. 5), when the HT temperature reached 770 °C, a large number of granular crystals appeared in the sample. However, when the HT temperature increased to 810 °C, short needle-like crystals began to appear, coexisting with  $\text{Ti}_5\text{O}_9$  granular crystals. When the HT temperature reached 890 °C, most of the  $\text{Ti}_5\text{O}_9$  granular crystals disappeared and became needle-like  $\text{TiO}_2$  crystals. The P4 sample undergoes crystalline transformation from  $\text{Ti}_5\text{O}_9$  crystals to  $\text{TiO}_2$  crystals during the HT process.

As shown in Fig. 3, the band at approximate  $472\text{ cm}^{-1}$  corresponds to the bending vibrations of the bridging oxygen bonds of  $\text{SiO}_4$  tetrahedron.<sup>10, 11</sup> Based on

the previous report by Jung and Sohn,<sup>10</sup> Raman band at approximately  $585\text{ cm}^{-1}$  is assigned to the  $[\text{AlO}_6]$ -octahedron. The bands located at approximately  $895$  and  $1070\text{ cm}^{-1}$  correspond to  $Q^1_{\text{Si}}$  (superscript refers to the number of bridged oxygen) and  $Q^3_{\text{Si}}$ , respectively.<sup>12</sup> In the P4 sample, the band at  $1070\text{ cm}^{-1}$  is not present because of the high concentration of  $\text{P}_2\text{O}_5$ .<sup>13</sup> Based on the previous report by Yadav and Singh, the characteristic symmetric stretching of the orthophosphate groups is normally found at approximately  $970\text{ cm}^{-1}$ .<sup>14</sup> For sample P2 and P4, the band at  $973\text{ cm}^{-1}$  corresponds to the characteristic vibration of  $\text{PO}_4^{3-}$  tetrahedra, representing the environment of phosphorus.<sup>15</sup> The sharp band located at  $959\text{ cm}^{-1}$  in P4 is attributed to  $\text{LiMgPO}_4$  crystalline clusters, which was consistent with the XRD results.<sup>16</sup> The Raman band corresponding to  $\text{PO}_4^{3-}$  evolves significantly with the increase of  $\text{P}_2\text{O}_5$  concentration.

In this work, no evident diffraction peak in P0, P2, and P4 was observed after isothermal HT at  $610\text{ }^\circ\text{C}$  (Fig. 2). However, Figs. 4A, 4D and 5A shows that the hole size of erosion increases with the gradual increase of  $\text{P}_2\text{O}_5$  content. In general, the addition of  $\text{P}_2\text{O}_5$  in the silicate glass would result in phase separation. The formation of these pits and holes can be attributed to the preferential attack of  $\text{HNO}_3$  on the phosphate-rich phase with weak acid resistance.<sup>17</sup> Combined with P-element mapping (Fig. 7), the phosphate agglomeration area and eroded pores are similar, further indicating that  $\text{P}_2\text{O}_5$  promotes phase separation. Based on the XRD pattern of the P4 sample ( $890\text{ }^\circ\text{C}$  for 2h) and Scherer formula, the calculated average grain size of the  $\text{LiMgPO}_4$  crystals in the sample is  $56.5\text{ nm}$ , which is consistent with the result of the

high-resolution image in the TEM (Fig. 7).

Evidently, two types of crystals co-exist in the amorphous glass matrix, one is a cluster-like crystal and the other is a needle-like crystal. Notably the needle-like crystals are randomly oriented in the glass matrix. Therefore, their maximum length can be observed only if a needle is by chance oriented along the needle axis. Cutting the needles in an arbitrary direction during TEM specimen preparation, leads to shorter fragments observed in projection. The extreme case occurs if a needle crystal is oriented perpendicularly to the cutting plane: then, the cross-section can be observed.<sup>7</sup> Based on the element mapping results, Ti are primarily concentrated in needle-like crystals; P and Mg are primarily concentrated in cluster-like crystals, and Al and Si are primarily presented in the glass matrix. Based on the above mentioned analysis, the needle-like crystals are rutile TiO<sub>2</sub>, and the cluster-like crystals are LiMgPO<sub>4</sub>.

As demonstrated by Ryerson and Mysen,<sup>18, 19</sup> the role of P<sub>2</sub>O<sub>5</sub> on the structure of silicate glass depends on the degree of polymerization. From the point of view of crystal chemistry, the ionic field strength  $F$  can be described as follows,<sup>20</sup>

$$F = \frac{Z}{r^2} \quad (1)$$

where  $Z$  and  $r$  are the valence and radius of ionic, respectively. P<sup>5+</sup> ion has a higher ionic field strength than Si<sup>4+</sup> ion (43.2 compared with 23.8).<sup>21-24</sup> The high field strength of the P<sup>5+</sup> ion attracts more O<sup>2-</sup> ions around, which relax and disturb the silicate glass network because of the various interstitial or modifying cations.<sup>25</sup>

Simultaneously,  $P^{5+}$  is a pentavalent network-forming cation, and electroneutrality is ensured only if one of the four oxygen ions around the  $P^{5+}$  ion is doubly bonded to the central  $P^{5+}$  cation. The double bond in the  $PO_4$  tetrahedra is shorter in length than the other three single bonds (0.1424 nm compared with 0.1595 nm), which results in the asymmetry of the  $PO_4$  tetrahedron and disturbs the bonding in the silicate network. In addition,  $Mg^{2+}$  and  $Li^+$  cations are likely to be included in the phosphate-rich phase because  $P^{5+}$  ion has a higher ionic field strength and greater tendency to shielding. Under this circumstance, phase separation likely occurs with P and Mg-enriched phase forming in the glass matrix. In the study of J. W. Cao *et al.*, a similar phenomenon also appeared; the P and Mg-enriched phase was formed from the glass matrix, and  $Mg_3(PO_4)_2$  crystals were formed, which served as the nuclei to favour the cordierite precipitation.<sup>26</sup> Moreover, similar phenomenon was reported in fluorapatite glass ceramics, in which Ca and P-enriched droplets are formed in the glass matrix.<sup>27,</sup>

28

Based on the XRD results, with the increase of  $P_2O_5$  in the system, silicate crystals disappeared, phosphate crystals appeared, and titanate crystals were transformed into rutile crystals. With the increase of  $P_2O_5$  content, the amount of  $PO_4$  in the glass network increases, and more cations are enriched in the P-rich phase. When the sample with 4 mol%  $P_2O_5$  (P4) was heat treated at 890 °C for 2 h, phosphate and rutile were separately formed in the P-rich and Ti-rich regions. When needle-like rutile crystals with a large L/D ratio appeared, the hardness of the P4 sample

significantly increased from 6.08 GPa to 7.14 GPa.

Therefore, with the increase of  $P_2O_5$  content, the number of  $PO_4^{3-}$  in the glass increased. Consequently, its ability to compete for  $Mg^{2+}$ ,  $Li^+$ , and other cations was enhanced. Finally, titanate crystal ( $MgTi_2O_5$ ) can not be observed when 4 mol%  $P_2O_5$  is introduced. The  $Ti_5O_9$  crystals appear simultaneously with  $LiMgPO_4$  crystals and transform to rutile  $TiO_2$  crystals at high temperature. Moreover, rutile crystals precipitate in the form of needle-like crystals with a large L/D ratio, and the length reaches more than 300 nm. Furthermore, the Vickers hardness of the P4 sample was significantly increased to 7.14 GPa.

## 5. Conclusions

In this work, as the  $P_2O_5$  content gradually increased from 0 to 4%,  $T_g$  of the sample gradually increased from 580 °C to 638 °C, The silicate crystals and titanate crystals in the sample disappeared successively, and the phosphate crystals and rutile crystals gradually appeared. Meanwhile, needle-like rutile crystals with high aspect ratio were grown from the  $SiO_2-Al_2O_3-MgO-TiO_2$  system by adding appropriate amount of  $P_2O_5$ . Under high ionic field strength of  $P^{5+}$ ,  $Mg^{2+}$  and  $Li^+$  preferentially moved toward the phosphorous-rich regions, forming spontaneous phase separation, in which the  $LiMgPO_4$  was formed in the glass matrix. Thus, the cations decreased in the glass matrix and Ti-rich region. In this work, the needle-like rutile with a large L/D ratio was grown from the Ti-rich region in the sample with  $P_2O_5$  up to 4 mol%

under HT at 890 °C for 2 h. Moreover, the large L/D ratio of needle-like crystals significantly increased the hardness from 6.08 GPa to 7.14 GPa. Similar to other fiber reinforced composites, this needle-like crystals provided a new strategy to improve the mechanical properties of glass ceramics.

### Acknowledgement

This work is financially supported by the National Natural Science Foundation of China (61975156) and Hubei Natural Science Foundation (2020CFB641).

### References

1. Budd MI. Sintering and crystallization of a glass powder in the MgO–Al<sub>2</sub>O<sub>3</sub>–SiO<sub>2</sub>–ZrO<sub>2</sub> system. *J. Mater. Sci.* 1993; 28: 1007-1014.
2. Song L, Wu J, Li Z, Hao X, Yu Y. Crystallization mechanisms and properties of  $\alpha$ -cordierite glass–ceramics from K<sub>2</sub>O–MgO–Al<sub>2</sub>O<sub>3</sub>–SiO<sub>2</sub> glasses. *J. Non-Cryst. Solids.* 2015; 419: 16-26.
3. Wange P, Höche T, Rüssel C, Schnapp JD. Microstructure-property relationship in high-strength MgO–Al<sub>2</sub>O<sub>3</sub>–SiO<sub>2</sub>–TiO<sub>2</sub> glass-ceramics. *J. Non-Cryst. Solids.* 2002; 298: 137-145.
4. Dittmer M, Müller M, Rüssel C. Self-organized nanocrystallinity in MgO–Al<sub>2</sub>O<sub>3</sub>–SiO<sub>2</sub> glasses with ZrO<sub>2</sub> as nucleating agent. *Mater. Chem. Phys.* 2010; 124: 1083-1088.
5. Wange P, Höche T, Rüssel C, Schnapp JD. Microstructure-property relationship in

- high-strength MgO–Al<sub>2</sub>O<sub>3</sub>–SiO<sub>2</sub>–TiO<sub>2</sub> glass-ceramics. *J. Non-Cryst. Solids*. 2002; 298: 137-145.
6. Han L, Song J, Lin C, et al. Crystallization, structure and properties of MgO–Al<sub>2</sub>O<sub>3</sub>–SiO<sub>2</sub> highly crystalline transparent glass-ceramics nucleated by multiple nucleating agents. *J. Eur. Ceram. Soc.* 2018; 38: 4533-4542.
7. Höland W, Ritzberger C, Apel E, et al. Formation and crystal growth of needle-like fluoroapatite in functional glass-ceramics. *J. Mater. Chem.* 2008; 18: 1318–1332.
8. Bansal NP. Mechanical behavior of silicon carbide fiber-reinforced strontium aluminosilicate glass–ceramic composites. *Mater. Sci. Eng.* 1997; A231: 117–127.
9. Yin S, Hasegawa H, Maeda D, Ishitsuka M, Sato T. Synthesis of visible-light-active nanosize rutile titania photocatalyst by low temperature dissolution–reprecipitation process. *J. Photochem. Photobiol. A.* 2004; 163: 1-8.
10. Jung SS, Sohn I. Crystallization control for remediation of an Fe<sub>2</sub>O<sub>3</sub>-rich CaO–SiO<sub>2</sub>–Al<sub>2</sub>O<sub>3</sub>–MgO EAF waste slag. *Environ. Sci. Technol.* 2014; 48: 1886-1892.
11. Mulder CAM. Defect structures in silica glass. *J. Non-Crystal.Solids.* 1987; 95: 303-310.
12. Mysen BO, Virgo D, Scarfe CM. Relations between the anionic structure and viscosity of silicate melts–A Raman spectroscopic study. *Am. Mineral.* 1980;

- 48: 690-710.
13. Mcmillan PF, Poe BT, Gillet P, Reynard B. A study of SiO<sub>2</sub> glass and supercooled liquid to 1950 K via high-temperature Raman spectroscopy. *Geochim. Cosmochim. Acta.* 1994; 58: 3653-3664.
14. Yadav AK, Singh P. A review of the structures of oxide glasses by Raman spectroscopy. *RSC Advances.* 2015; 5: 67583-67609.
15. Popović L, Manoun B, Waal Dd, Nieuwoudt MK, Comins JD. Raman spectroscopic study of phase transitions in Li<sub>3</sub>PO<sub>4</sub>. *J. Raman Spectrosc.* 2003; 34: 77-83.
16. Ariane K, Tamayo A, Chorfa A, Rubio F, Rubio J. Effect of P<sub>2</sub>O<sub>5</sub> and Al<sub>2</sub>O<sub>3</sub> on crystallization, structure, microstructure and properties of Li<sub>2</sub>O–MgO–Al<sub>2</sub>O<sub>3</sub>–SiO<sub>2</sub>–TiO<sub>2</sub>–ZrO<sub>2</sub> glass ceramics. *Bol. Soc. Esp. Cerám. Vidr.* 2020. <https://doi.org/10.1016/j.bsecv.2020.08.004>.
17. Liu S, Lan S, Tao H, Yue Y. Self-limited growth of nanocrystals in phosphosilicate melts during cooling. *J. Eur. Ceram. Soc.* 2019; 39: 3876-3882.
18. Ryerson FJ, Hess PC. The role of P<sub>2</sub>O<sub>5</sub> in silicate melts. *Geochim. Cosmochim. Ac.* 1980; 44: 611-624.
19. Mysnn BRO, RyBnson FJ, Virgo D. The structural role of phosphorus in silicate melts. *Am. Mineral.* 1981; 66: 106-117.
20. McMillan PW. Glass-Ceramics. *Academic Press, Inc. New York*, 1979.
21. O'Donnell MD, Watts SJ, Law RV, Hill RG. Effect of P<sub>2</sub>O<sub>5</sub> content in two series

- of soda lime phosphosilicate glasses on structure and properties – Part I: NMR. *J. Non-Cryst. Solids*. 2008; 354: 3554-3560.
22. Oliveira JM, Correia RN, Fernandes MH. Effect of SiO<sub>2</sub> on amorphous phase separation of CaO–P<sub>2</sub>O<sub>5</sub>–SiO<sub>2</sub>–MgO glasses. *J. Non-Cryst. Solids*. 2000; 273: 59-63.
23. Höche T, Moiescu C, Avramov I, Rüssel C. Microstructure of SiO<sub>2</sub>-Al<sub>2</sub>O<sub>3</sub>-CaO-P<sub>2</sub>O<sub>5</sub>-K<sub>2</sub>O-F- Glass Ceramics. 2. Time dependence of apatite crystal growth. *Chem. Mater*. 2001; 13: 1320-1325.
24. Chen X, Hench LL, Greenspan D, Zhong J, Zhang X. Investigation on phase separation, nucleation and crystallization in bioactive glass-ceramics containing fluorophlogopite and fluorapatite. *Ceram. Int*. 1998; 24: 401-410.
25. Mirsaneh M, Reaney IM, Hatton PV, Bhakta S, James PF. Effect of P<sub>2</sub>O<sub>5</sub> on the early stage crystallization of K-fluorrichterite glass–ceramics. *J. Non-Cryst. Solids*. 2008; 354: 3362-3368.
26. Cao JW, Li YH, Liang KM. Effect of P<sub>2</sub>O<sub>5</sub> on evolution of microstructure of MgO–Al<sub>2</sub>O<sub>3</sub>–SiO<sub>2</sub> glass ceramics. *Adv. Appl. Ceram.* 2013; 108: 352-357.
27. Moiescu C, Jana C, Rüssel C. Crystallization of rod-shaped fluoroapatite from glass melts in the system SiO<sub>2</sub>–Al<sub>2</sub>O<sub>3</sub>–CaO–P<sub>2</sub>O<sub>5</sub>–Na<sub>2</sub>O–K<sub>2</sub>O–F<sup>-</sup>. *J. Non-Cryst. Solids*. 1999; 248: 169-175.
28. Höche T, Moiescu C, Avramov I, Rüssel C. Microstructure of SiO<sub>2</sub>-Al<sub>2</sub>O<sub>3</sub>-CaO-P<sub>2</sub>O<sub>5</sub>-K<sub>2</sub>O-F<sup>-</sup> glass ceramics. 1. Needlelike versus isometric

morphology of apatite crystals. *Chem. Mater.* 2001; 13: 1320-1325.

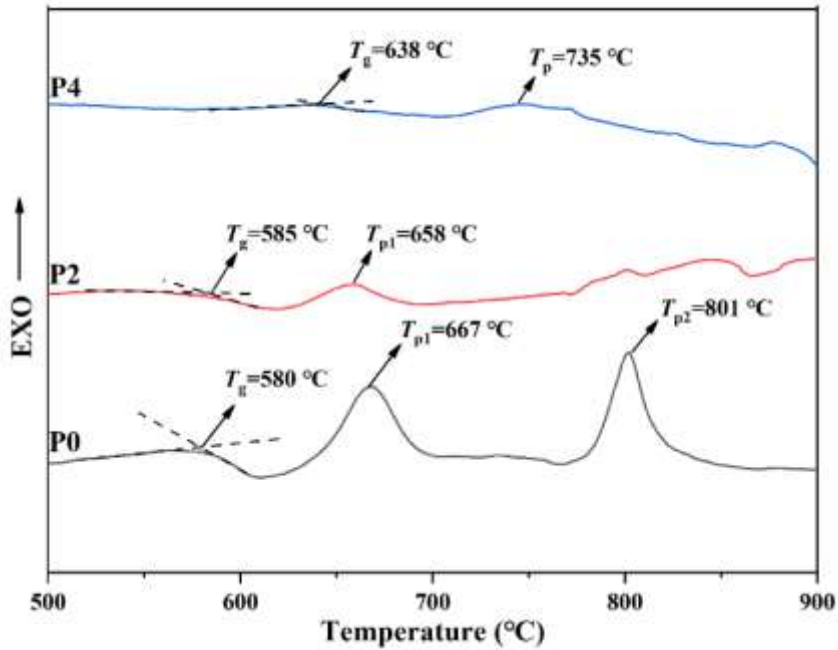


Fig. 1 DSC curves of P0, P2, and P4 glasses.

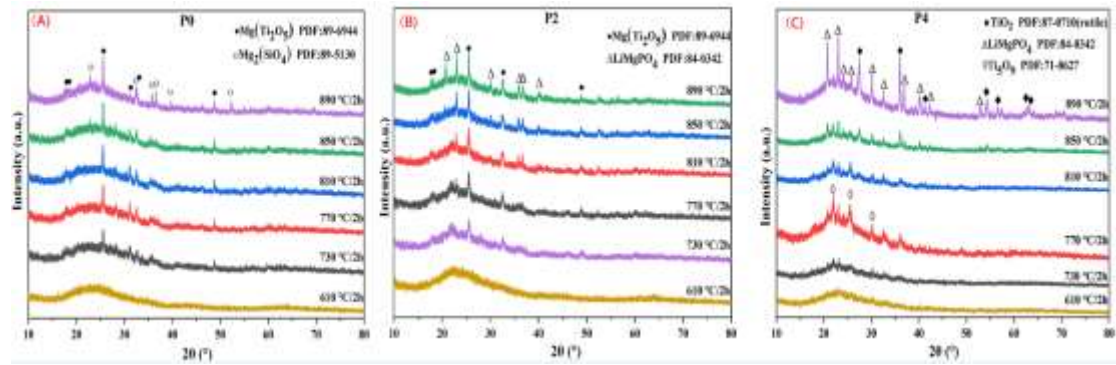


Fig. 2 XRD patterns of (A) P0, (B) P2, and (C) P4 glasses heat treated at various temperatures for 2 h.

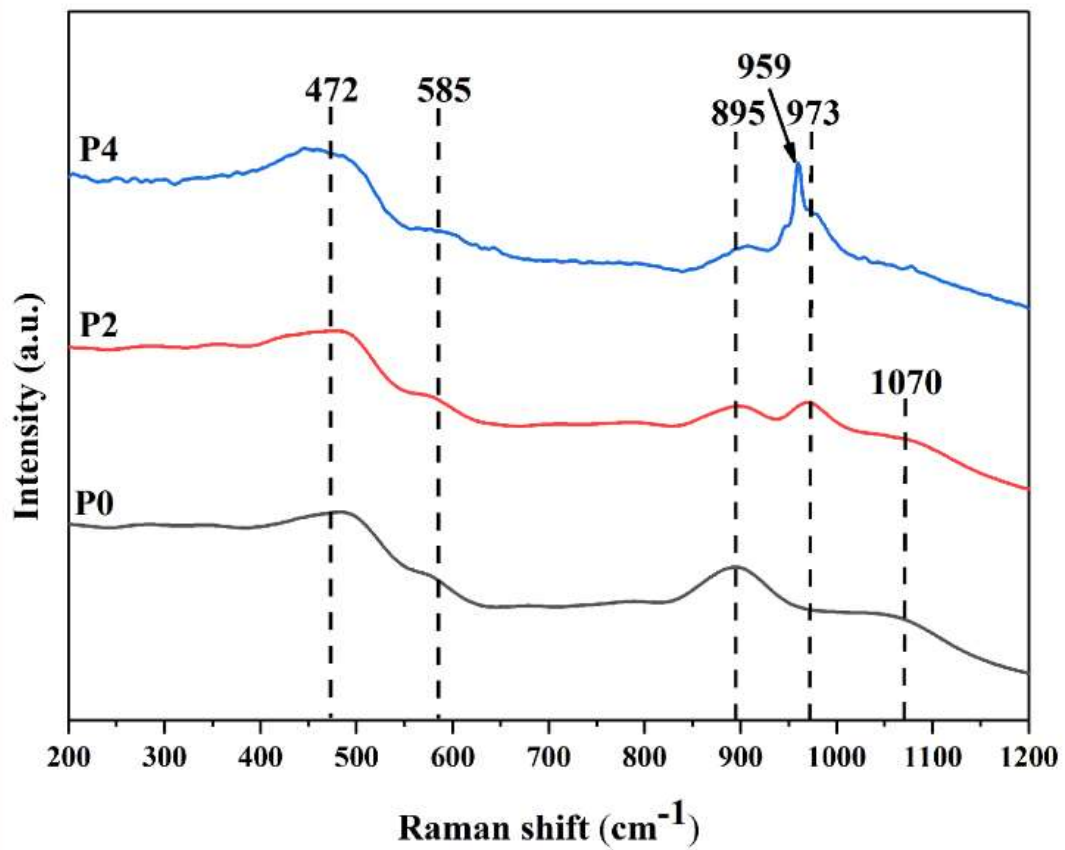


Fig. 3 Raman spectra of as-quenched P0, P2, and P4 glasses.

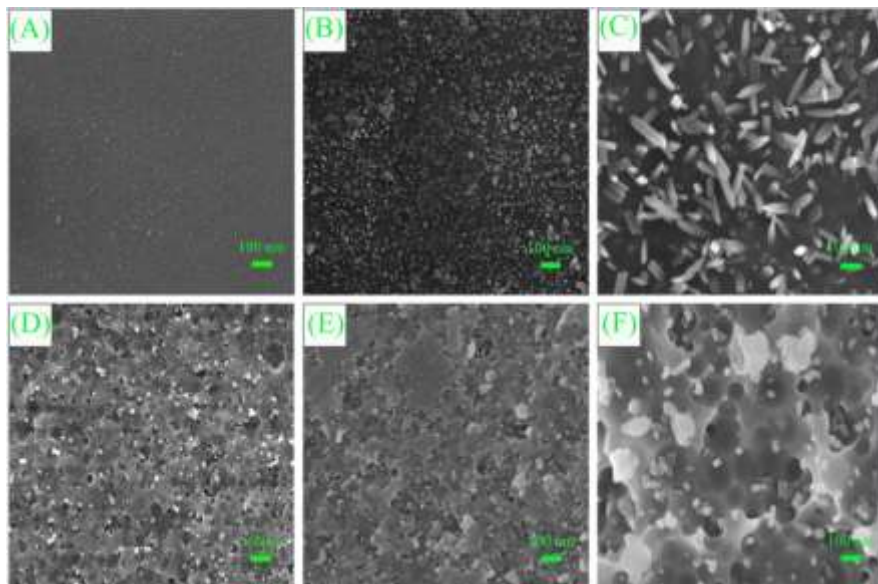


Fig. 4 SEM images of P0 and P2 glasses heat-treated at various temperatures for 2 h.

(A) P0, 610 °C. (B) P0, 730 °C. (C) P0, 890 °C. (D) P2, 610 °C. (E) P2, 730 °C.

(F) P2, 890 °C.

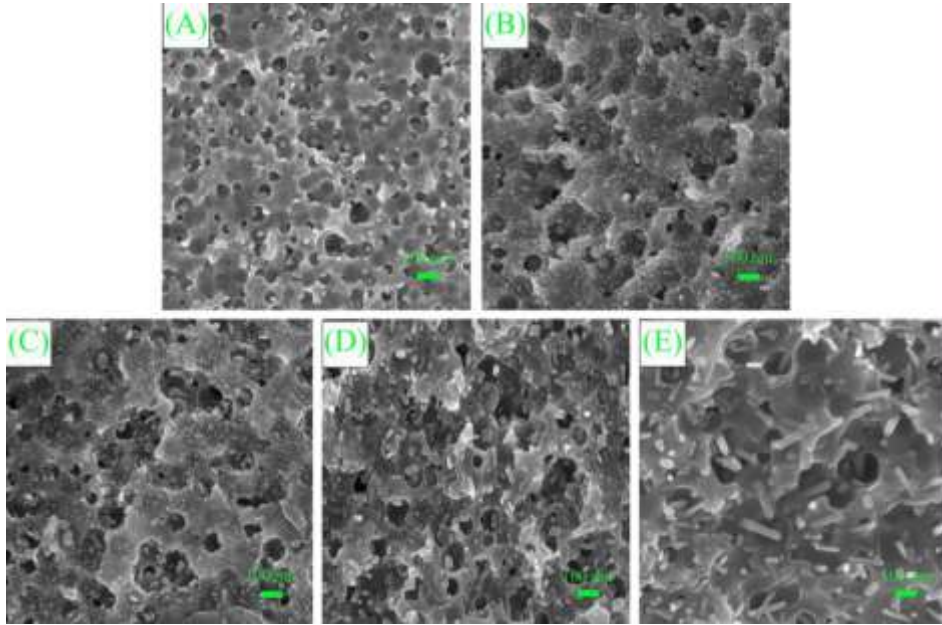


Fig. 5 SEM images of P4 glass heat-treated at (A) 610 °C, (B) 730 °C, (C) 770 °C, (D) 810 °C, and (E) 890 °C for 2 h.

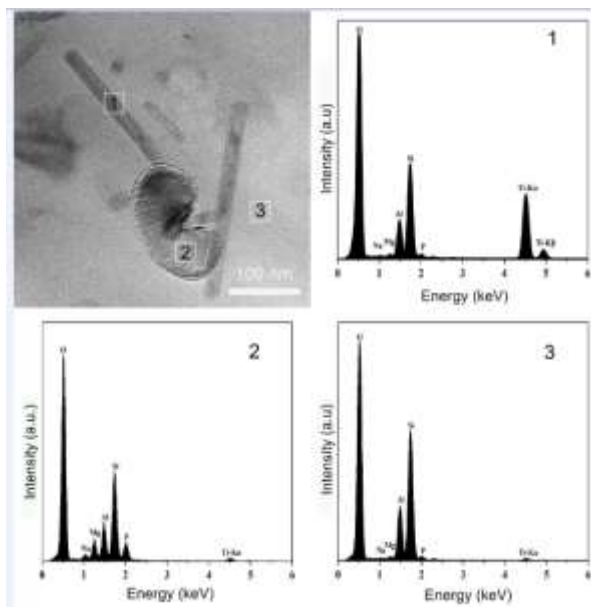


Fig. 6 TEM image and corresponding EDS elements analysis at needle-like crystal (point 1), cluster-like crystal (point 2) and glass substrate (point 3).

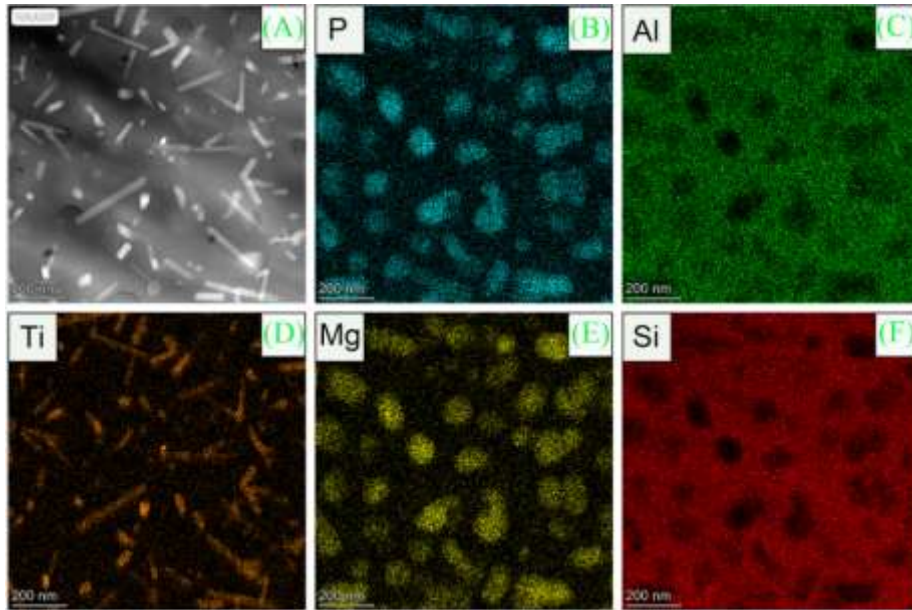


Fig. 7 (A) TEM bright field micrograph and (B–F) corresponding EDS elements mapping of the P4 glass sample heat-treated at 890 °C for 2 h.

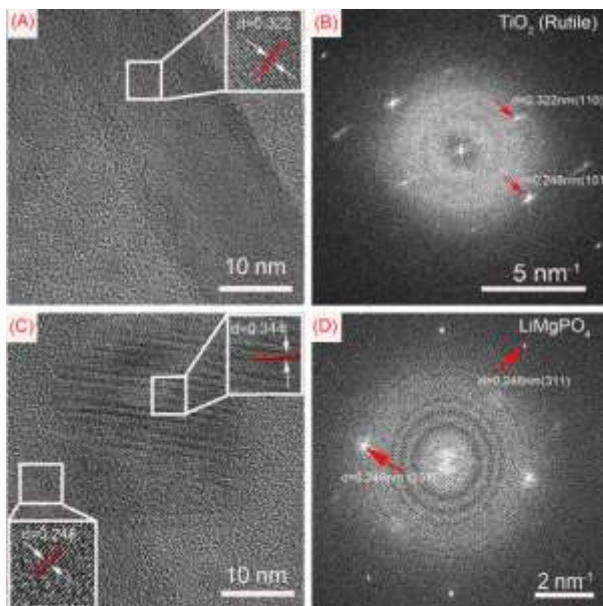


Fig. 8 High resolution TEM images and selected area electron diffraction pattern of needle-like (A and B) and cluster-like (C and D) crystals in the P4 glass sample heat-treated at 890 °C for 2 h. Inset of the TEM images are the enlarged lattice fringe of crystals.

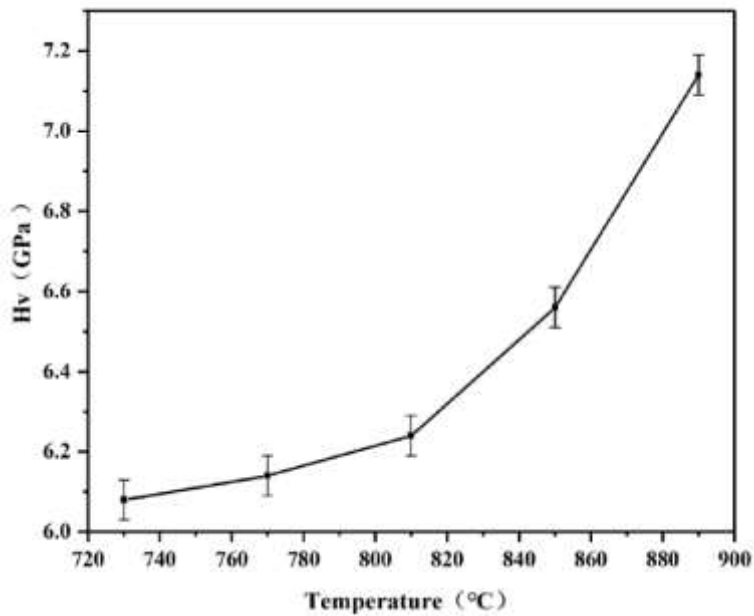


Fig. 9 Vickers hardness of the P4 sample heat treated at different temperatures. The error bar is  $\pm 0.05$  GPa.

#### **Declaration of Competing Interest**

The authors declare that they have no known competing financial interests or personal relationships that could have appeared to influence the work reported in this paper.

#### **Summary of Novel Conclusions**

The needle-like rutile crystals with a large L/D ratio were grown from the Ti-rich region in the MgO-Al<sub>2</sub>O<sub>3</sub>-SiO<sub>2</sub>-TiO<sub>2</sub> glass. After precipitation of the rutile TiO<sub>2</sub> and LiMgPO<sub>4</sub> crystals, the hardness of glass was increased significantly from 6.08 GPa to 7.14 GPa.